Journal of Materials Chemistry A

ROYAL SOCIETY OF CHEMISTRY

PAPER

View Article Online
View Journal | View Issue

Cite this: J. Mater. Chem. A, 2023, 11, 25020

A single-phase gadolinium-doped ceria cathode for highly efficient CO_2 electrolysis†

Ahmad Shaur, [a] Michel Drazkowski, [a] Shaochen Zhu, [a] Bernard Boukamp [b] and Henny J. M. Bouwmeester *[acd]

High-temperature solid-oxide CO_2 electrolysers enable high-efficiency conversion of electrical energy to valuable fuels and chemicals and as such facilitate a sustainable-energy technology. Conventional cermet-based fuel electrodes used in such solid-oxide cells (SOCs) like nickel–yttria-stabilized zirconia (Ni–YSZ) suffer from morphological degradation and destructive carbon deposition. In recent years, there has been an increasing interest in employing single-phase ceria-based fuel electrodes, which are known to exhibit excellent carbon deposition resistance. Under sufficiently reducing conditions, doped ceria (substituted with trivalent cations such as samarium or gadolinium to generate mobile oxygen vacancies) becomes a mixed ionic–electronic conductor, showing appreciable electronic conductivity. Here, we show for the first time stable high performance in CO_2 electrolysis using a ceria-based SOC. The single full cell incorporating a 10 mol% gadolinium-doped ceria (GCO) fuel electrode delivers a current density as high as 1.51 A cm^{-2} at 800 °C during pure CO_2 electrolysis, which is the best electrode performance reported to date among all-ceramic cathode materials. We demonstrate that the electrode performance in CO_2 electrolysis is linked with the electronic conductivity, and hence, with the electronic charge carrier concentration in GCO. The results of the present work pave the way for development of robust, nickel-free SOCs for direct CO_2 electrolysis.

Received 6th July 2023
Accepted 3rd November 2023

DOI: 10.1039/d3ta03977c

rsc.li/materials-a

Introduction

In the global effort to develop efficient and carbon-neutral alternatives to fossil fuels, SOCs currently attract extensive attention due to their high faradaic efficiencies, wide fuel flexibility, and low pollutant emission. They can be operated reversibly, converting chemical fuels to electricity (fuel cell mode) and *vice versa* (electrolysis cell mode), at high efficiencies and with zero emissions.[1,2] Operating in the electrolysis cell mode, SOCs which can be thermally integrated with downstream chemical processing can be employed to convert surplus electricity generated from renewables to a wide range of storable synthetic fuels and chemicals.[3] In particular, there is a growing worldwide interest in the direct electrochemical conversion of the greenhouse gas CO_2.[4,5] Fig. 1 demonstrates the overall reaction scheme for CO_2 electrolysis in a solid oxide electrolysis cell (SOEC), where CO_2 is converted to CO at the cathode (fuel electrode), while the formed oxygen ion migrates *via* the electrolyte to the anode (air/oxygen electrode), where it is oxidized to O_2.[6,7]

In Kröger–Vink notation, the CO_2 reduction reaction may be written as

$$CO_{2(g)} + V_O^{\cdot\cdot} + 2e' \rightarrow CO_{(g)} + O_O^{\times}$$

where $V_O^{\cdot\cdot}$, $O_O^{\times}$, and e' denote a doubly ionized oxygen vacancy, a regular lattice oxygen and an electron, respectively. $V_O^{\cdot\cdot}$ and e' are the charge carriers being transported to the surface reaction site, where gaseous CO_2 is reduced to CO. The state-of-the-art SOEC cathode is the nickel–yttria stabilized zirconia (Ni–YSZ) cermet electrode.[8,9] Here, the electrode reaction is confined to the near vicinity of the triple-phase boundary (3PB), where the gas phase, the ionic conductor and the catalytically active metal phase are in simultaneous contact with each other. However, Ni–YSZ electrodes are inherently redox unstable and prone to issues like re-oxidation, morphological degradation, and coking.[10,11] Moreover, a flow of safety gas (reducing gas, *e.g.*, H_2/CO) premixed with the CO_2 feed gas needs to be supplied to the electrode during start-up and/or to avoid (re-)oxidation of Ni to NiO in the event of an incidental shut-down.[12] To overcome these drawbacks or limitations, researchers still endeavour to

[a]Electrochemistry Research Group, MESA+ Institute for Nanotechnology, University of Twente, P.O. Box 217, 7500 AE, Enschede, The Netherlands. E-mail: h.j.m.bouwmeester@utwente.nl

[b]Inorganic Materials Science Group, MESA+ Institute for Nanotechnology, University of Twente, P.O. Box 217, 7500 AE, Enschede, The Netherlands

[c]CAS Key Laboratory of Materials for Energy Conversion, Department of Materials Science and Engineering, University of Science and Technology of China, Hefei, 230026, P. R. China

[d]Forschungszentrum Jülich GmbH, Institute of Energy and Climate Research-IEK-1, Leo- Brandt-Str. 1, D-52425, Jülich, Germany

† Electronic supplementary information (ESI) available. See DOI: https://doi.org/10.1039/d3ta03977c

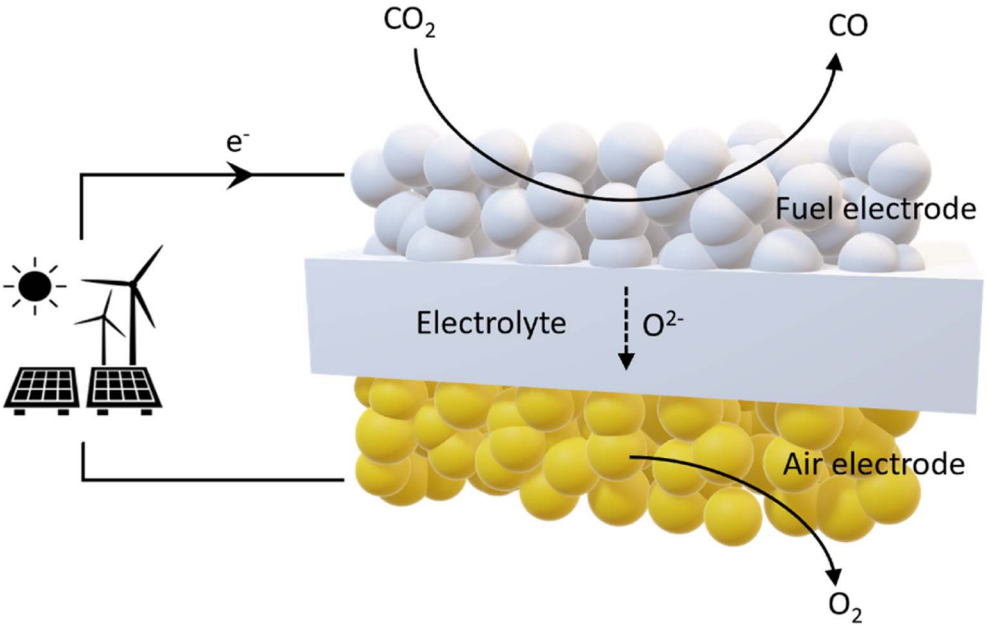

Fig. 1 Schematic diagram showing the general operating principle of a solid oxide electrolysis cell (SOEC) for CO_2 electrolysis. High-temperature SOEC's offer efficient storage of renewable energy in the form of CO and other chemical fuels.

find alternative electrode materials, thereby focusing on mixed ionic–electronic conducting oxides (MIECs) with high stability under reducing conditions.[8] The use of an MIEC as electrode material extends the active area over the entire electrode surface, thus potentially enhancing the overall reaction rate.[13] Amongst others, mixed-conducting perovskite-type oxides such as $La_{0.75}Sr_{0.25}Cr_{0.5}Mn_{0.5}O_{3-\delta}$ (LSCrMn),[7,14,15] $La_xSr_{1-x}TiO_{3-\delta}$ (LST),[16–18] $SrTi_{0.3}Fe_{0.7}O_{3-\delta}$ (STF),[19] $La_{0.6}Sr_{0.4}FeO_{3-\delta}$ (LSF),[20,21] $Sr_2Fe_{1.5}Mo_{0.5}O_{6-\delta}$ (SFMo),[9] $Sr_2Fe_{1.4}Mn_{0.1}Mo_{0.5}O_{6-\delta}$ (SFMnMo),[9] and $Sr_2Fe_{1.5}Mo_{0.5}O_{6-\delta}F_{0.1}$ (F-SFMo),[22] have been tested for use as a cathode for CO_2 electrolysis.[6,23,24] Infiltration, fluorine-doping, and/or *in situ* exsolution of reducible transition metal cations have been applied to enhance the performance of the perovskites electrodes.[1,6,8] For some of the perovskite-structured electrodes strontium segregation and subsequent carbonation have been found to induce passivation, resulting in performance degradation over time.[25–27] The best performance in the open literature has been reported to date for the fluorine-doped SFM fuel electrode, incorporated in a 250 μm-thick $La_{0.9}Sr_{0.1}Ga_{0.8}Mg_{0.2}O_{3-\delta}$ (LSGM) electrolyte-supported cell, showing a current density of 1.38 A cm^{-2} at an applied potential of 1.5 V at 800 °C, using pure CO_2 as feed gas.[22]

Besides its use as electrolyte or as diffusion barrier layer, doped ceria (typically gadolinium- or samarium-doped ceria) is commonly employed as an additive to SOC fuel electrodes, either as an (impregnated) catalyst[28] or as a dispersed phase to enhance the overall 3PB length.[9,29–31] Acceptor-doped ceria exhibits electronic conductivity to become a mixed ionic–electronic conductor under reducing conditions.[32,33] Chueh *et al.*[34] used ceria-metal cermet electrodes to investigate the kinetics of the H_2 oxidation reaction. The authors showed that the reaction pathway is dominated by electrocatalysis at the oxide/gas interface (2PB) with only a minimal contribution from the oxide/metal/gas boundaries (3PBs).[34] Nenning *et al.*[35] found excellent kinetics for thin-film single-phase Gd-doped ceria (GCO) electrodes tested in both H_2/H_2O and CO/CO_2 atmospheres using electrochemical impedance spectroscopy on symmetrical cells, while Skafte *et al.*[36] showed selective CO_2 to CO conversion for thin-film ceria-based electrodes well beyond the thermodynamic carbon deposition threshold. These studies clearly point towards the potential of single-phase doped ceria for use as fuel electrode. Here, we demonstrate for the first time exceptional performance of single-phase porous GCO electrodes in pure CO_2 electrolysis, achieving a current density of 1.51 A cm^{-2} in electrolyte-supported cells operated at 1.5 V at 800 °C. We further demonstrate that the performance arises in response of the high electronic conductivity in the ceria-based electrode being linked with the Nernstian chemical potential associated with the applied overpotential. Symmetrical cell tests are conducted to probe the electrode polarization and the effective electrolyte resistance.

Results and discussion

Electrolysis cell and performance

Here, an electrolyte-supported SOEC was fabricated by screen-printing a 20 μm-thick GCO ($Gd_{0.1}Ce_{0.9}O_{2-\delta}$) layer on a 150 μm-thick 8 mol% yttria-stabilized zirconia (8YSZ) electrolyte disc (Fig. S1†). Screen-printed $La_{0.6}Sr_{0.4}Co_{0.2}Fe_{0.8}O_{3-\delta}$ (LSCF) was used as the oxygen electrode. A dense 2 μm-thin diffusion-barrier layer of GCO obtained by pulsed layer deposition (PLD) was applied between the 8YSZ electrolyte and the LSCF electrode to prevent the formation of secondary phases. Different CO/CO_2 gas mixtures were fed to the GCO cathode, whereas

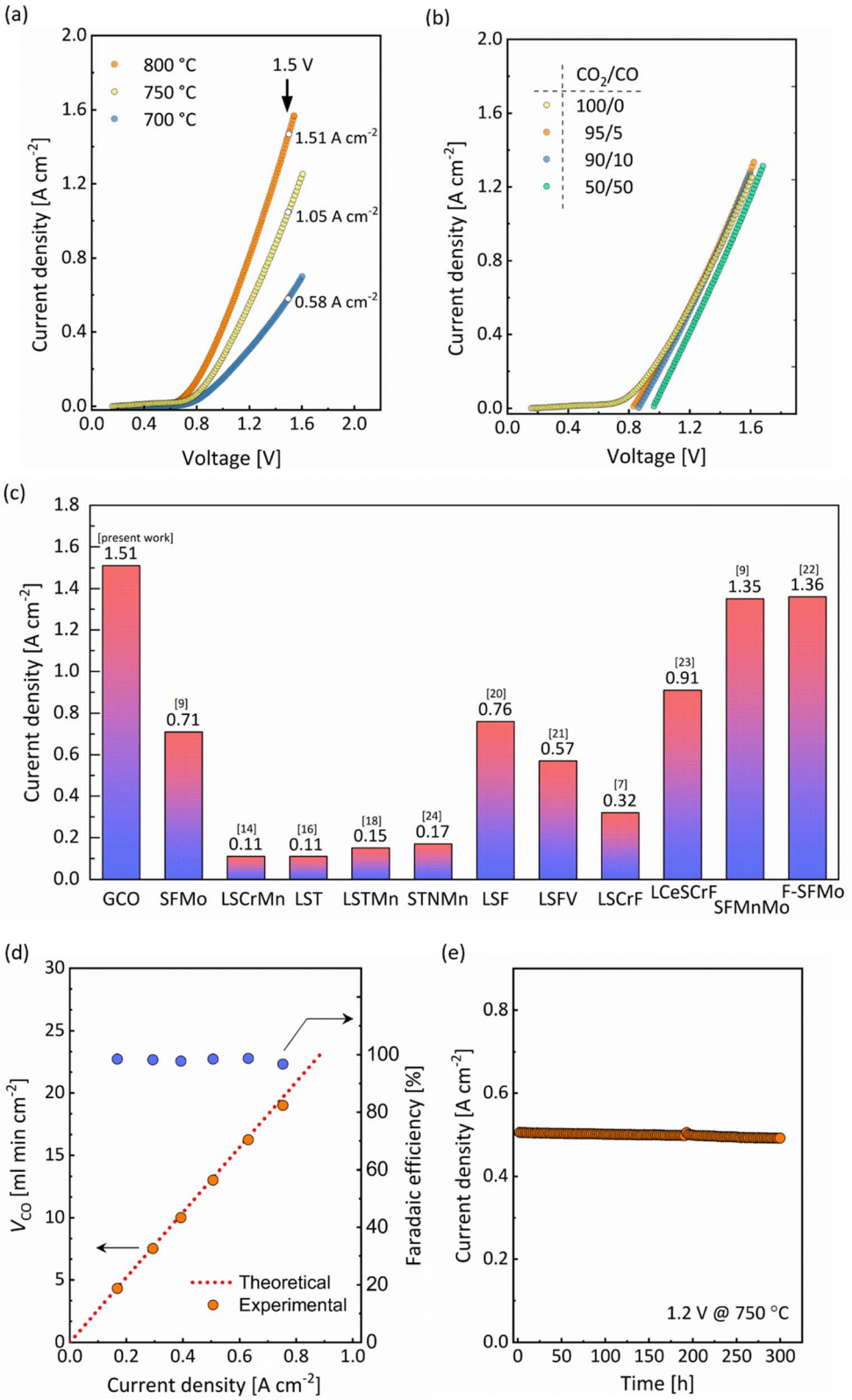

Fig. 2 Single-cell performance for the electrolyte-supported SOEC LSCF|GCO|8YSZ|GCO, incorporating a single-phase GCO cathode (a) *I–V* curves for pure CO_2 electrolysis collected at different temperatures. (b) *I–V* curves of the cell operated at 750 °C in different CO_2/CO atmospheres. (c) Comparison of the cell performance at 800 °C and at 1.5 V under pure CO_2 electrolysis with that of cells based on different single-phase oxide cathode materials: $La_{0.6}Sr_{0.4}FeO_{3-\delta}$ (LSF),[20] $Sr_2Fe_{1.5}Mo_{0.5}O_{6-\delta}$ (SFMo),[9] $Sr_2Fe_{1.4}Mn_{0.1}Mo_{0.5}O_{6-\delta}$ (SFMnMo),[9] $Sr_2Fe_{1.5}Mo_{0.5}O_{6-\delta}F_{0.1}$ (F-SFMo),[22] $La_{0.6}Sr_{0.4}TiO_{3-\delta}$(LST),[16] $La_{0.6}Sr_{0.4}Ti_{0.8}Mn_{0.2}O_{3-\delta}$ (LSTMn),[18] $La_{1.2}Sr_{0.8}Cr_{0.5}Mn_{0.5}O_4$ (LSCrMn),[14] $La_{0.6}Sr_{0.4}Fe_{0.5}V_{0.5}O_{3-\delta}$ (LSFV),[21] $La_{0.70}Sr_{0.3}Cr_{0.5}Fe_{0.5}O_{3-\delta}$ (LSCrF),[7] $Sr_{0.95}Ti_{0.80}Nb_{0.10}Mn_{0.10}O_{3-\delta}$ (STNMn)[24] and $La_{0.65}Ce_{0.05}Sr_{0.3}Cr_{0.5}Fe_{0.5}O_{3-\delta}$ (LCeSCrF).[23] (d) CO production rate and corresponding faradaic efficiency as a function of applied current density of the cell operated at 750 °C under pure CO_2 electrolysis. (e) Long-term durability test at 1.2 V and 750 °C under pure CO_2 electrolysis.

synthetic air (21% oxygen with nitrogen balance) was supplied to the anode side of the cell. Fig. 2a shows current–voltage (*I–V*) curves for pure CO_2 electrolysis in the range of 700–800 °C, while Fig. 2b shows corresponding curves, at 750 °C, in atmospheres with different CO_2/CO volume ratios. There is virtually no hysteresis in the *I–V* curves, which were recorded from open-circuit voltage (OCV) to about 1.6 V, indicating high reversibility of the cell within the constraints of the experiment. A current density as high as 1.51 A cm^{-2} at 1.5 V, at 800 °C, is found for pure CO_2 electrolysis, which to our knowledge is the highest value reported to date for single-phase oxide electrode materials (Fig. 2c). Fig. 2d shows the CO production rate (V_{CO}) and faradaic efficiency as a function of current density, at 750 °C, for pure CO_2 electrolysis. The value of V_{CO} increases to 18.0 ml min^{-1} cm^{-2} as the current density increases to 0.75 A cm^{-2} (which is reached at a cell voltage of 1.32 V). The faradaic efficiency remains close to 100%. Next, we proceeded to perform pure CO_2 electrolysis, at 750 °C, at an applied voltage of 1.2 V. A stable performance is found for 300 h (Fig. 2e). *Post mortem* scanning electron microscopy (SEM) did not show any sign of degradation of the electrode microstructure (Fig. S1c†). The obtained results in this study clearly demonstrate that GCO holds great promise for stable and selective CO_2 electrolysis.

Electrochemical impedance spectroscopy

Electrochemical impedance spectroscopy (EIS) was performed on electrolyte-supported symmetrical cells, GCO|8YSZ|GCO, at different temperatures in CO_2/CO 50/50, and in different CO_2/CO atmospheres at 750 °C. To this end, GCO layers 20 μm thick were screen-printed on both sides of a 150 μm-thick 8YSZ electrolyte disc. A typical impedance spectrum obtained from measurements is shown in Fig. 3a. All impedance spectra were analyzed with an effective equivalent circuit model incorporating a transmission line model (TLM) for the electrode

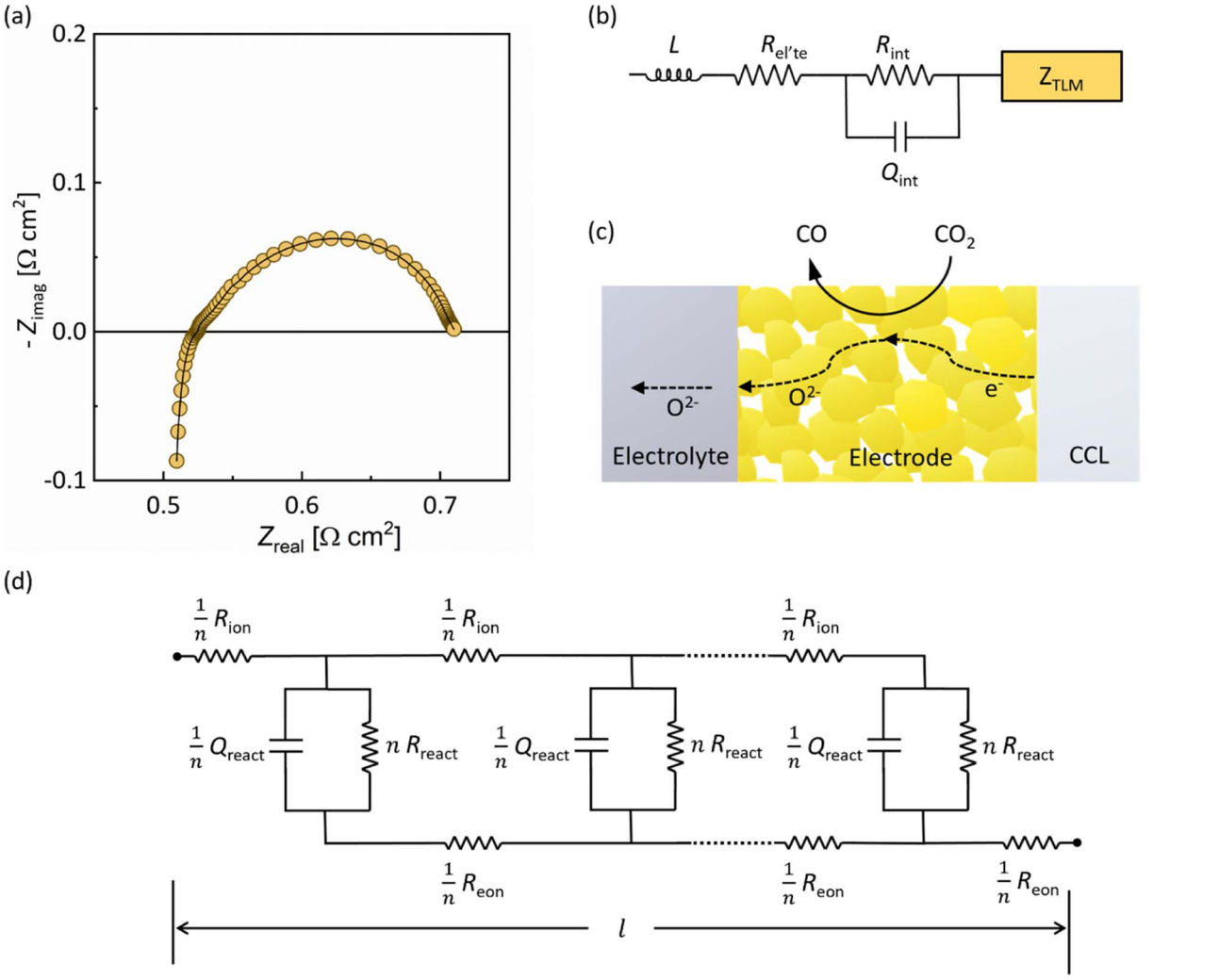

Fig. 3 Equivalent circuit fitting of the impedance response of the electrolyte-supported symmetrical cell GCO|8YSZ|GCO. (a) Typical impedance spectrum recorded at 750 °C in CO_2/CO 50/50 atmosphere. The solid line is from equivalent circuit fitting. (b) Effective equivalent circuit used for fitting. The impedance response of the GCO electrodes is modeled by a transmission line model (TLM) with associated impedance Z_{TLM}. (c) Schematic of ion transport, electron transport and electrochemical reaction in the porous GCO electrode (CCL = current collecting layer). (d) Transmission line model (TLM) for the homogeneously structured GCO electrode.

responses (Fig. 3b). The TLM consists of two rails accounting for the transport of electrons and oxygen ions to and from discrete reaction sites (Fig. 3c and d). These reaction sites are distributed along the thickness of the porous GCO electrode. The descriptive parameters for transport are the effective ionic resistance (R_{ion}) and the effective electronic resistance (R_{eon}), which in addition to their corresponding intrinsic values of GCO, are affected by the porosity (ε) of the electrode and the tortuosity (τ) of the conduction pathways. Electrode parameters and equations used for estimating values of R_{ion} and R_{eon} for fitting are provided in Table S1.† The coupling between ionic and electron charge carriers through the electrochemical reaction is represented by the parallel combination of a surface reaction resistance (R_{react}) and a constant phase element or CPE (Q_{react}), with admittance $Y_{CPE}(\omega) = Q_{react}(j\omega)^{\alpha_{react}}$ where Q_{react} and $0 < \alpha_{react} < 1$ are characteristic parameters and ω is the angular frequency.[37] For a symmetrical cell, the impedance response of the electrodes is twice that of a single electrode. Throughout this text, electrode parameters obtained from equivalent circuit fitting are presented for individual electrodes.

The expression for the impedance of the TLM model as was first derived in the PhD thesis by De Boer[38] is given by

$$Z_{TLM} = R_p + (R_s - 2R_p)\frac{\coth(k)}{k} + 2R_p\frac{1}{k\sinh(k)} \quad (1)$$

where $R_p = R_{ion}R_{eon}/(R_{ion} + R_{eon})$, $R_s = R_{ion} + R_{eon}$ and $k = \sqrt{R_s(1 + Y_{CPE}R_{react})/R_{react}}$. In derivation of eqn (1), gas phase diffusion limitations in the porous electrode are ignored. The quantities R_{ion}, R_{eon}, R_{react} (Ω cm^2) and Q_{react} (F s$^{\alpha_{react}-1}$ cm^{-2}) correspond to the whole electrode thickness. It may be shown that eqn (1) is mathematically equivalent to that derived by Bisquert *et al.*[39] Additional elements in the equivalent circuit shown in Fig. 3b include: (i) an inductance (L) related to the wiring and instruments, (ii) the ionic resistance of the 8YSZ

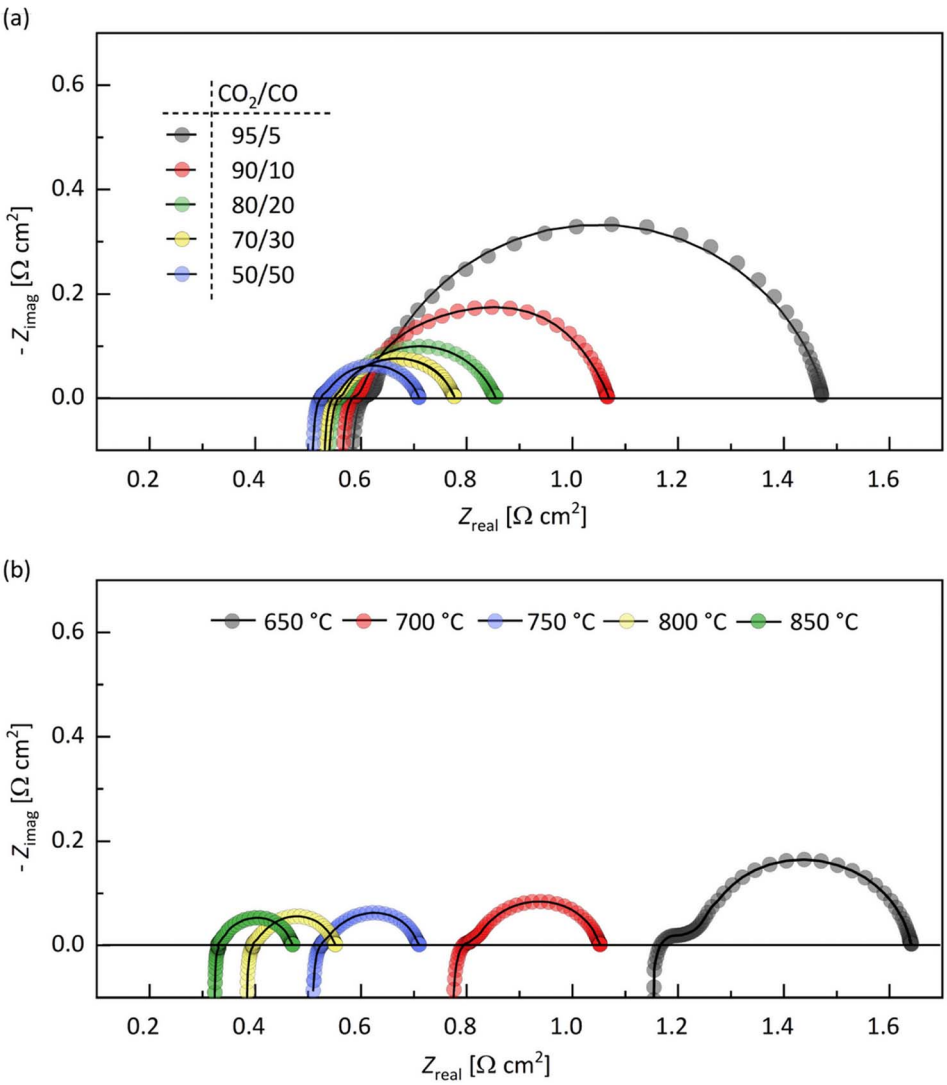

Fig. 4 Impedance spectra of the electrolyte-supported symmetrical cell GCO|8YSZ|GCO. Spectra recorded at (a) 750 °C in different CO_2/CO gas mixtures and (b) at different temperatures in CO_2/CO 50/50. The solid lines are from equivalent circuit fitting. Corresponding resistance values from fitting are given in Tables S4 and S5 (ESI†), respectively.

electrolyte ($R_{el'te}$), (iii) the ion transfer resistance (R_{int}) and (iv) associated CPE (Q_{int}) of the interface between electrolyte and electrode layer. Excellent fits of the impedance spectra are obtained over the entire frequency range (Fig. 3a and 4). To avoid over-parameterization, values for R_{ion} and R_{eon} were estimated from data of electrical conductivity (discussed below). Best-fit parameters obtained from equivalent circuit fitting of the impedance spectrum shown in Fig. 3a are listed in Table S2.†

The value of the high-frequency cut-off resistance, R_∞, in impedance spectra is normally solely determined by the electrolyte resistance, $R_{el'te}$. At constant temperature, however, R_∞ in this work is found to decrease with decreasing CO_2/CO ratio (Fig. 4a and Table S3†), *i.e.*, with the drop of pO_2, which indicates that the GCO electrode contributes to R_∞. This is in accordance with the n-type electronic conductivity of GCO under reducing conditions, increasing with decreasing pO_2. The high-frequency cut-off resistance becomes $R_\infty = R_{el'te} + 2R_p$, where R_p corresponds to the high-frequency limit of eqn (1). The calculated values of $R_{el'te}$ in different CO_2/CO gas mixtures, at 750 °C, remain essentially constant (within 2%; Table S3†), as expected. Fig. S2† compares the Arrhenius plot of the ionic conductivity of 8YSZ calculated using data of $R_{el'te}$ (Table S4†) obtained from equivalent circuit fitting of the impedance spectra measured at different temperatures in CO_2/CO 50/50 with literature data. The overall matching is good, though some discrepancy is noted at the highest temperatures. It can, therefore, not be excluded that $R_{el'te}$ is a lumped parameter containing contributions of bulk ionic conductivity and possibly interfacial transfer.

At DC conditions ($\omega \rightarrow 0$), the resistance of the transmission line model ($Z_{TLM}|_{\omega\rightarrow 0}$) can be calculated by means of eqn (1) using $k = \sqrt{R_s/R_{react}}$. The contribution of R_{int} to the area-specific resistance ASR ($=R_{int} + Z_{TLM}|_{\omega\rightarrow 0}$) of the GCO electrode is within range 2–7%, depending on temperature and applied CO_2/CO gas mixture (Tables S3 and S4†). The activation energy of 0.88 ± 0.06 eV estimated from the Arrhenius plot of $1/R_{int}$ (Fig. S3a†) is regarded as the energy barrier for interfacial oxygen ion transfer between 8YSZ and GCO. Values of the effective capacitance associated with the CPE, calculated using $C_{int} = Q_{int}^{1/\alpha_{int}} R_{int}^{(1-\alpha_{int})/\alpha_{int}}$,[40] range from 0.40×10^{-3} F cm^{-2} at 650 °C to 1.12×10^{-3} F cm^{-2} at 850 °C in CO_2/CO 50/50 (Fig. S3c†). These values are typical for interfacial capacitances at solid/solid boundaries, generally of the order of 10^{-3} F cm^{-2} to 10^{-5} F cm^{-2}.[13,41] From the observed α_{int} values ($0.83 < \alpha_{int} < 0.87$) we learn that Q_{int} approaches ideal capacitive behavior.

A prominent contribution to the ASR of the GCO electrode originates from the surface reaction resistance R_{react}, depending on temperature and CO_2/CO gas mixture (Fig. S4a and b†). Note that when the resistances associated with ionic and electronic transport can be ignored, it follows that ASR = $R_{int} + R_{react}$. The relatively large values observed for C_{react}, from 0.10 F cm^{-2} at 650 °C to 0.65 F cm^{-2} at 850 °C in CO_2/CO 50/50 (Fig. S4c†) as calculated by conversion of Q_{react} ($C_{react} = Q_{react}^{1/\alpha_{react}} R_{react}^{(1-\alpha_{react})/\alpha_{react}}$), are attributed to the bulk chemical capacitance of GCO, due to its ability to store electrical charge in response to changes in the oxygen chemical potential.[40] Values of α_{react} are found to vary between $0.80 < \alpha_{react} < 0.87$. The interfacial capacitance of the GCO electrode/gas interface and the dielectric capacitance will in principle also contribute to the apparent value of C_{react}, though their impact is judged to be negligible.

The expression for the chemical capacitance of GCO can by derived from the change of oxygen stoichiometry with change in oxygen chemical potential (*i.e.*, inverse thermodynamic factor). Assuming local charge electroneutrality and dilute charge carrier concentrations, this expression can be evaluated as[42]

$$C_{chem} = \frac{4VF^2}{RT}\left(\frac{1}{c_{ion}} + \frac{4}{c_{eon}}\right)^{-1} \quad (2)$$

where V is the sample volume, and c_{ion} and c_{eon} are the defect concentrations of ionic and electronic charge carriers, respectively. Parameters F, R and T have their usual meanings. The charge carriers in GCO under reducing conditions are mobile oxygen vacancies and localized electrons, so-called small polarons. From eqn (2), it is obvious that C_{chem} is predominated by the concentration of the minority charge carrier. Examining the data in Fig. S4b and d† indicate that the gas phase dependencies of C_{react} and $1/R_{react}$ are close to $\propto pO_2^{-1/4}$, suggesting that both quantities are determined by the minority electron concentration in GCO. This power law dependence of the electron concentration on pO_2 is seen in the 'Brouwer region' of the equilibrium defect diagram of GCO where the oxygen vacancy concentration is fixed by the Gd-dopant concentration, *i.e.*, provided that the enthalpy for oxygen reduction is constant,

$$2O_O^\times + 2Ce_{Ce}^\times \rightarrow V_O^{\cdot\cdot} + 2Ce'_{Ce} + \frac{1}{2}O_{2(g)} \quad (3)$$

where Ce'_{Ce} represents the Ce^{3+} cations, or small electron polarons, and $Ce_{Ce}^\times$ represents the Ce^{4+} cations. Fig. S5† shows that the electron carrier concentration, $[Ce'_{Ce}]$, determined using the chemical capacitance values exhibits good agreement with the expected $pO_2^{-1/4}$ dependence. Furthermore, excellent agreement is found with values of $[Ce'_{Ce}]$ evaluated from oxygen nonstoichiometry data reported by Bishop *et al.*[43] (Fig. S5†).

Comparison with literature values reported for other single-phase oxide electrode materials investigated for potential use in high-temperature CO_2 electrolysis shows that GCO exhibits the lowest ASR values in a wide temperature range (Fig. 5).[44–48] In calculation of the ASR values the GCO electrode at different temperatures in CO_2/CO 50/50 and, at 750 °C, in different CO_2/CO gas mixtures, the DC resistance of the TLM model ($Z_{TLM}|_{\omega\rightarrow 0}$) has been evaluated from the fitted parameters (see Tables S3 and S4,† respectively). It is recalled that these parameters correspond to the whole electrode thickness (d_{exp}) instead of being specified per unit thickness. Thicker electrodes reduce the activation overpotential, through their larger surface area, but increase the ohmic losses. The optimal electrode thickness (d_{opt}) can be evaluated by plotting $Z_{TLM}|_{\omega\rightarrow 0}$ as a function of electrode thickness (d), which requires rescaling of the fitted parameters R_{ion}, R_{eon} and R_{react} with factor d/d_{exp}. Fig. S6† shows that $Z_{TLM}|_{\omega\rightarrow 0}$ at 750 °C in CO_2/CO 50/50 exhibits a shallow minimum at around 32 μm. The precise value of d_{opt} can be calculated using,

$$d_{opt} = d_{exp}\sqrt{\frac{R_{react}}{R_s}}\ln\left[1+\sqrt{\frac{R_s}{R_p}}+\sqrt{\left(1+\sqrt{\frac{R_s}{R_p}}\right)^2-1}\right] \quad (4)$$

This equation can be obtained by setting the partial derivative of $Z_{TLM}|_{\omega\to 0}$ with respect to d to zero.[38] Experimental validation of the ASR values at different GCO electrode thicknesses is currently in progress and will be subject of a forthcoming paper.

Importance of electron carrier concentration to cell performance

To elucidate the role of electronic conductivity or, equally, the electronic carrier concentration on the performance of GCO as electrode material for CO_2 electrolysis, the total electrical conductivity (σ_{tot}) of GCO was measured at different temperatures as a function of pO_2, using different O_2/N_2 and CO_2/CO gas mixtures. The obtained data extend the data set previously measured for the related composition $Sm_{0.15}Ce_{0.85}O_{2-\delta}$ by Haile *et al.*[41] to higher temperatures and clearly demonstrate that GCO is an ionic conductor under moderately oxidizing conditions and becomes a mixed conductor under reducing conditions (Fig. 6). The experimental data can be fitted to $\sigma_{tot} = \sigma_{ion} + \sigma_{eon} = \sigma_{ion} + \sigma^0_{eon}pO_2{}^m$, assuming that the concentration of oxygen vacancies and, hence, the ionic conductivity (σ_{ion}) in GCO is fixed by the Gd-dopant concentration. At moderate temperatures, the electronic contribution to the conductivity exhibits an $m = -1/4$ power law dependence on pO_2 as may be inferred from defect chemical considerations assuming ideal solution behavior. At higher temperatures, the absolute value of m begins to deviate from this dependence to slightly higher values, *i.e.*, from $m = -0.249 \pm 0.008$ at 650 °C to $m = -0.291 \pm 0.011$ at 850 °C (Table S5†). Consistent with previous findings,[49–51] these observations can be accounted for by a decrease in the enthalpy of reduction of non-stoichiometric doped ceria due to defect interactions, easing the formation of electrons and oxygen vacancies upon lowering pO_2.[50,51] A detailed discussion on the electrical conductivity of GCO is beyond the scope of this paper and will be presented elsewhere.[52]

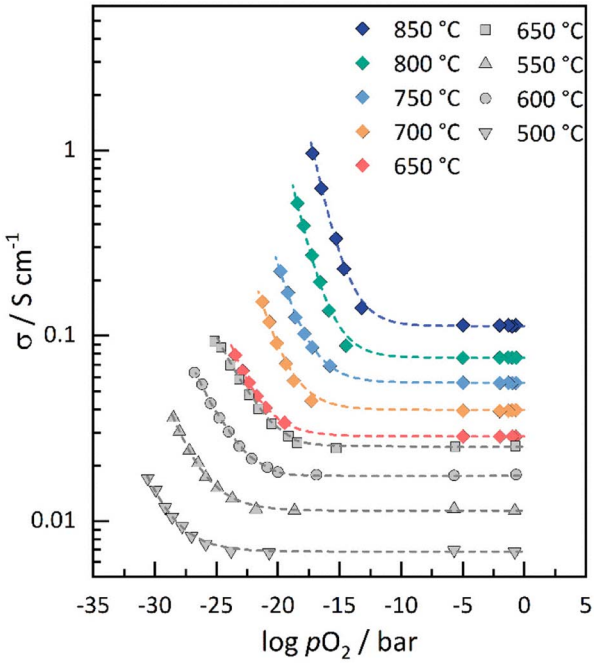

Fig. 6 Total electrical conductivity of GCO at different temperatures as a function of oxygen partial pressure. Also shown are data of the total electrical conductivity for $Sm_{0.15}Ce_{0.85}O_{2-\delta}$, taken from Lai *et al.*[41] Dashed lines represent the fit of the experimental data to $\sigma_{tot} = \sigma_{ion} + \sigma^0_{eon}pO_2{}^m$.

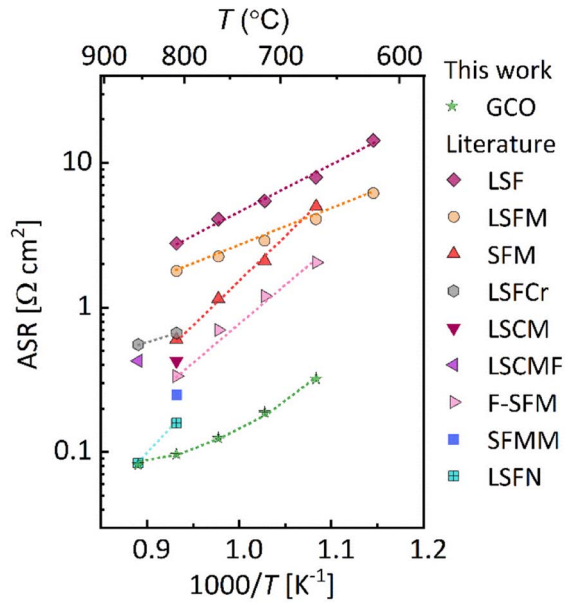

Fig. 5 Comparison of the area-specific resistance (ASR) of different single-phase oxide cathode materials used for high-temperature CO_2 electrolysis: $La_{0.6}Sr_{0.4}FeO_{3-\delta}$ (LSF),[21] $La_{0.6}Sr_{0.4}Fe_{0.95}Mo_{0.05}O_{3-\delta}$ (LSFMo),[45] $Sr_2Fe_{1.5}Mo_{0.5}O_{6-\delta}$ (SFMo),[9] $La_{0.3}Sr_{0.7}Cr_{0.3}Fe_{0.7}O_{3-\delta}$ (LSCrF),[47] $La_{1.2}Sr_{0.8}Co_{0.4}Mn_{0.6}O_4$ (LSCoMn),[43] $La_{0.9}Sr_{0.8}Co_{0.4}Mn_{0.6}O_{3.9-\delta}F_{0.1}$ (F-LSCoMn),[44] $Sr_2Fe_{1.5}Mo_{0.5}O_{6-\delta}F_{0.1}$ (F-SFMo),[22] $Sr_2Fe_{1.4}Mn_{0.1}Mo_{0.5}O_{6-\delta}$ (SFMnMo),[9] $La_{0.6}Sr_{0.4}Fe_{0.8}Ni_{0.2}O_{3-\delta}$ (LSFN).[46] The gas phase composition is CO_2/CO 50/50 in all cases.

Fig. 7a shows the electrolysis current density of the full cell (synthetic air) LSCF|GCO|8YSZ|GCO (CO_2/CO), at 750 °C, in different CO_2/CO atmospheres alongside with the bulk electronic conductivity of GCO at this temperature as a function of the effective pO_2 within the GCO electrode. The latter is estimated using the Nernst equation,[53–55]

$$E = \frac{RT}{4F}\ln\left(\frac{pO_2(\mathrm{GCO})}{pO_2(\mathrm{LSCF})}\right) \quad (5)$$

where E is the (*IR*-corrected) cell voltage, and pO_2 (GCO)and pO_2 (LSCF) are the effective oxygen partial pressures within the GCO and LSCF electrode, respectively. The implicit assumptions justifying its use in this study are that (i) the overpotential between the current collecting layer (CCL) and GCO is small, (ii) the overpotential at the GCO electrode/gas interface is much larger than that across the 8YSZ/GCO boundary, *i.e.*, $R_{react} \gg R_{int}$, (iii) the oxygen chemical potential is uniform within the GCO electrode, *i.e.*, bulk transport within GCO is assumed to be fast,

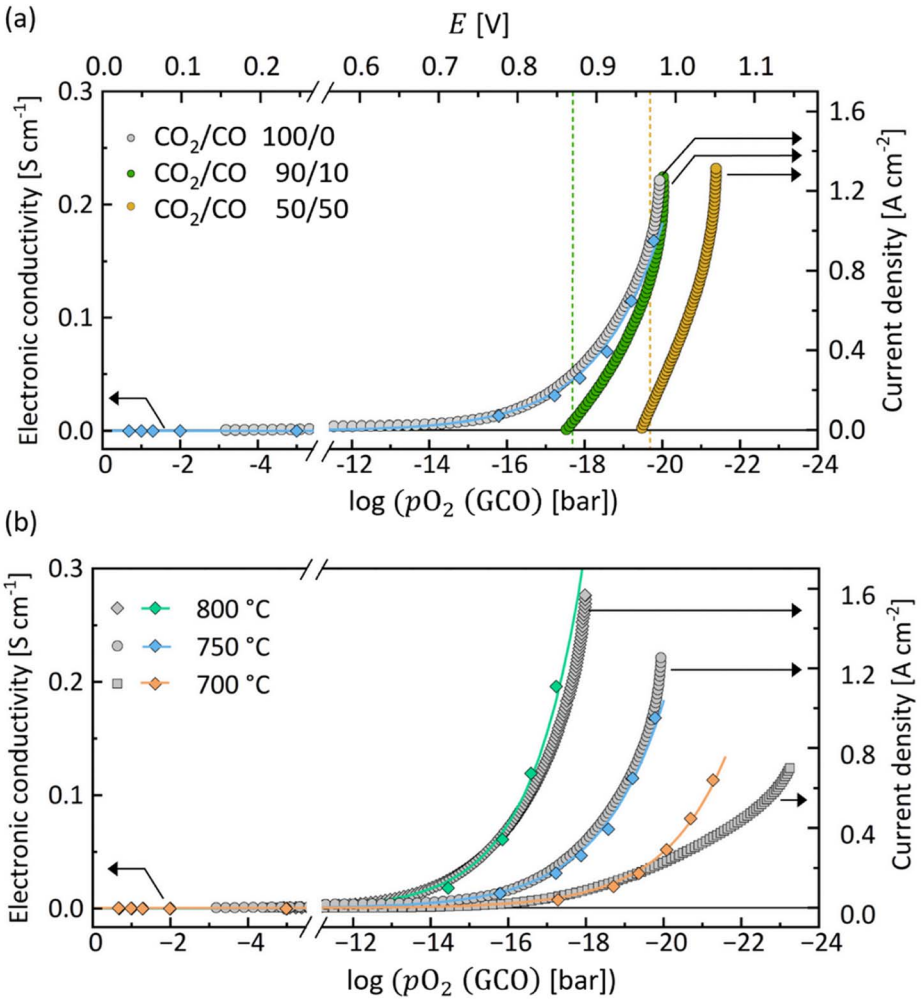

Fig. 7 Bulk electronic conductivity of GCO and electrolysis current density of the cell (synthetic air) LSCF|GCO|8YSZ|GCO (CO_2/CO) as functions of the (*IR*-corrected) cell voltage log(pO_2 (GCO)) (top axis) or effective pO_2 within the GCO electrode (bottom axis) in (a) different CO_2/CO atmospheres, at 750 °C, and (b) for pure CO_2 electrolysis at different temperatures. The dashed lines in (a) refer to the theoretical OCV values in corresponding gas mixtures. The effective pO_2 within the GCO electrode is calculated using Nernst's equation (eqn (5)).

and (iv) no significant polarization losses occur at the LSCF electrode. Note that the second assumption is validated to a certain degree by the corresponding results presented in Tables S3 and S4.† Equivalent circuit fitting of the data of impedance measurements at OCV confirms that the LSCF oxygen electrode, when being exposed to synthetic air, contributes less than 2% to the overall polarization resistance, R_{pol}, of the cell (Fig. S7 and Table S6†). Upon electrolyzing pure CO_2, at 750 °C, almost no increase in current density is found upon increasing the (*IR*-corrected) cell voltage below ~0.65 V (Fig. 7a). Beyond this cell voltage, a strong correlation exists between current density and electronic conductivity. Similar observations are obtained at temperatures at 800 °C and 700 °C (Fig. 7b). The loss of correlation between the current density and the electronic conductivity observed, at 700 °C, at the lowest pO_2 values may be due to the emergence of additional rate-limiting steps at these conditions. Note further from Fig. 7a that at 750 °C a bulk electronic conductivity of value 0.168 S cm^{-1} is sufficient to sustain a current density of 1 A cm^{-2}. The dashed lines in this figure refer to the theoretical OCV values in either CO_2/CO 90/10 or CO_2/CO 50/50. Electronic conductivity at OCV conditions in the latter gas mixtures has reached distinct values due to equilibration of the GCO electrode with the gas phase. Fig. 8 shows the CO_2 electrolysis current density, at 750 °C, as a function of electronic conductivity in different CO_2/CO atmospheres. An almost linear correlation between current density and electronic conductivity is found in each of the gas atmospheres. These results suggest that the electronic charge carrier plays an essential role in the reaction pathway of CO_2 dissociation on the GCO surface, noting that the electronic conductivity is proportional to the product of mobility and carrier concentration, while it may be assumed that the mobility is virtually constant within the experimental window. The latter is confirmed by plotting the electronic conductivity of GCO *versus* the associated Ce'_{Ce} localized electron concentration derived from literature oxygen non-stoichiometry data,[49] showing a linear relationship between both parameters (Fig. S8†).

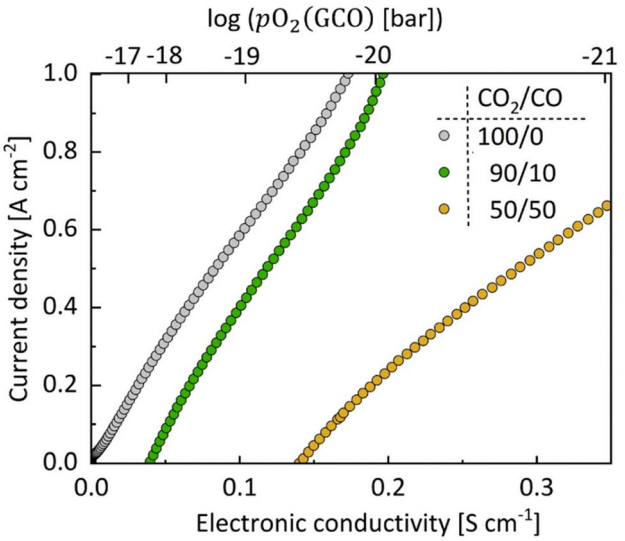

Fig. 8 CO_2 electrolysis current density at 750 °C as functions of log(pO_2 (GCO)) (top axis) or bulk electronic conductivity of GCO (bottom axis) in different CO_2/CO atmospheres. The effective pO_2 within the GCO electrode has been calculated from the applied (*IR*-corrected) cell voltage *via* Nernst's equation (eqn (5)). The associated bulk electronic conductivity is calculated using $\sigma_{eon} = \sigma^0_{eon} pO_2^{-m}$. Values of σ^0_{eon} and m obtained from fitting experimental data of the total conductivity (Fig. 6) are listed in Table S5.†

Above observations can be rationalized in terms of a simple reaction scheme for CO_2 dissociation on the GCO surface as has been proposed earlier by Feng *et al.*[55]

Step 1

$$Ce^{\times}_{Ce} + e'_{CCL} \rightarrow Ce'_{Ce} \quad (6)$$

Step 2

$$CO_{2(g)} + O^{\times}_{O} + Ce'_{Ce} \rightarrow CO'_{3,ad} + Ce^{\times}_{Ce} \quad (7)$$

Step 3

$$CO'_{3,ad} + Ce'_{Ce} + V^{\cdot\cdot}_{O} \rightarrow CO_{(g)} + 2O^{\times}_{O} + Ce^{\times}_{Ce} \quad (8)$$

where e'_{CCL} represents an electron from the metal current collecting layer (CCL) and $CO'_{3,ad}$ an adsorbed carbonate ion. It is assumed that the transport of mobile charge carriers within the GCO layer to the surface reaction site does not impose any rate limitations. Step 1 involves the electron transfer from the CCL to the GCO bulk. Step 2 is the chemisorption of CO_2 onto a surface oxygen ion. The chemisorption involves electron transfer from a small polaron site at the surface to the adsorbed CO_2 molecule, generating a surface monodentate carbonate species ($CO'_{3,ad}$). In reaction step 3, a second electron transfer from the oxide surface leads to dissociation of the carbonate intermediate and formation of gaseous CO. Here, we may speculate that step 2 is rate determining as it predicts, in line with the results presented in Fig. 8, a current which is proportional to both the concentration of Ce'_{Ce} and the partial pressure of CO_2 in the gas phase. However, our proposal contradicts with the work of Feng *et al.*[55] Using ambient pressure X-ray photoelectron spectroscopy (AP-XPS), these authors observed that the coverage of the surface carbonate intermediates on samarium-doped ceria ($Sm_{0.2}Ce_{0.8}O_{2-\delta}$) increases with the surface concentration of Ce'_{Ce}, as was found in an earlier study on pure ceria.[56] Based upon this observation, Feng *et al.*[55] postulated quasi-equilibration of the surface carbonate coverage due to a high rate constant for reaction step 2 relative to step 3. There is consensus in literature that CO_2 electrolysis on oxide surfaces proceeds *via* carbonate intermediates. In fact, various binding configurations of surface carbonates have been reported.[57] Noting that step 3 is a concerted reaction, our observations could equally well be explained by rate determining formation of a bidentate carbonate configuration (by adsorption of $CO'_{3,ad}$ onto a nearby oxygen vacancy site) prior to electron transfer and dissociation of the formed surface complex. Clearly more research is needed to unambiguously address the mechanism of CO_2 dissociation on ceria-based oxide surfaces.

Conclusions

Our findings support that doped ceria has a great promise for use as a fuel electrode for CO_2 electrolysis in SOECs. A current density of 1.51 A cm^{-2} has been achieved in pure CO_2 electrolysis using electrolyte-supported cells operated at 1.5 V at 800 °C. This performance exceeds that of other single-phase oxide cathodes currently reported in literature. It is believed that there is still scope for improvement of the performance by optimizing the microstructure, to enhance the exposed surface area, and electrode thickness. Furthermore, full cell designs with lower overall resistance than the electrolyte-supported cell used in this study can be considered. The almost-linear correlation of the current density with electronic conductivity observed in different CO_2/CO atmospheres suggests that electron transfer between ceria and adsorbed CO_2 is likely rate determining. However, more research is needed to unambiguously address the mechanism of CO_2 dissociation.

Experimental

Materials and cell fabrication

Dense 8 mol% yttria-stabilized zirconia (8YSZ) electrolyte substrates of 150 μm thickness were purchased from Kerafol (Germany). Precursor electrode powders of GCO ($Gd_{0.1}Ce_{0.9}O_{2-\delta}$) and LSCF ($La_{0.6}Sr_{0.4}Co_{0.2}Fe_{0.8}O_{3-\delta}$) were purchased from Fuelcellmaterials (USA). Electrode powder slurries were prepared by mixing 2 g precursor powder with 2 g dispersant (6 wt% ethyl-cellulose dissolved in terpineol) with a mortar and pestle before screen-printing onto the 8YSZ substrate. First, a 2 μm-thin GCO diffusion-barrier layer (between the LSCF electrode and 8YSZ substrate) was grown on one side of the 8YSZ substrate using PLD, employing a KrF laser (Lambda Physik, Germany) with a wavelength of 248 nm. The growth parameters of the GCO film were: laser repetition frequency 10 Hz, target–substrate distance 50 mm, substrate temperature 600 °C, fluency 2.5 J cm^{-2} and O_2 background pressure 10^{-3} mbar.

Subsequently, a GCO electrode layer was screen printed on the opposite side of the 8YSZ substrate, followed by drying at 100 °C for 1 h and annealing in air at 1200 °C for 3 h. Hereafter, the LSCF oxygen electrode was screen-printed onto the GCO barrier layer and annealed in air at 1000 °C for 3 h, resulting in the complete single full cell LSCF|GCO|8YSZ|GCO. Brush-painted gold functioned as current collecting layer (CCL) on both sides of the cell. The top surface of the GCO fuel electrode and the cross-section of the cell after annealing were examined using a scanning electron microscope (SEM, JEOL JSM-6010 LA, Japan). The thickness of the GCO electrode after sintering was 20 μm. Symmetrical cells GCO|8YSZ|GCO were prepared using procedures like those as described above.

Electrochemical testing

Electrochemical testing was accomplished using a home-made test rig. A single full cell was mounted onto an alumina test tube with a ceramic sealant (Ceramabond 552, Aremco Products Inc.). A flow of CO_2/CO was supplied to the GCO fuel electrode, while a flow of oxygen (balanced with nitrogen) was supplied to the LSCF oxygen electrode. For symmetrical cell testing, the same CO_2/CO gas mixture was supplied to both sides of the cell, which was mounted onto the test tube using a perforated alumina disc. Measurements were performed under various conditions. The total flow rates were 200 ml min^{-1} and in all cases the CO_2 utilization was less than 4% at all current densities. The concentration of gases was controlled by mass flow controllers (GF40, Brooks Instruments). *I–V* curves were collected by cyclic voltammetry from OCV to 1.6 V at a scan rate of 20 mV s^{-1} using a potentiostat (Gamry reference 3000, Gamry Instruments). The Faraday efficiency was evaluated by analyzing the fuel outlet gas using online gas chromatography (Compact GC 4.0, Interscience). The long-term durability of the full cell was tested at 1.2 V for 300 h supplying pure CO_2 to the GCO electrode and 21% oxygen (balanced with nitrogen) to the LSCF electrode. Impedance spectra of the full cell were recorded, at 750 °C, with CO_2/CO 90/10 supplied to the fuel side and different concentrations of oxygen to the oxygen side. Impedance spectra on symmetrical cells were recorded at different temperatures in CO_2/CO 50/50, and at 750 °C in different CO_2/CO gas mixtures. Impedance data were collected in the frequency range 10 mHz to 100 kHz frequency range and were validated by a Kramers–Kronig test using the Gamry Echem Analyst software package (Gamry Instruments). Equivalent circuit analysis of the impedance spectra was carried out using the ZView software package (Scribner Associates Inc.).

Electrical conductivity testing

Powders of GCO were pelletized by uniaxially pressing at 25 MPa followed by isostatic pressing at 400 MPa. Subsequently, the pellets were sintered at 1400 °C in air for 4 h with heating/cooling rates of 2 °C min^{-1}. The relative density of the pellets after sintering was 96.3% of the theoretical value as measured by Archimedes' method. Thin rectangular bars were cut out of the sintered pellets using a cutting machine (Secotom-50, Struers LLC). The obtained bars were ground by abrasive plates and subsequently polished (Tegramin-20, Struers LLC) to final dimensions 15 × 6 × 0.9 mm^3. Electrical conductivity data were collected by a standard four-probe dc technique using platinum wires (Fiaxell SOFC Technologies, 0.25 mm in diameter) wrapped around the bar to act as electrodes. Platinum ink (Fuelcellmaterials) was applied on the sample surface directly underneath the platinum wires. Prior to measurements, the bar was *in situ* annealed in synthetic air at 900 °C for 1 h to establish a proper adhesion between the platinum wires and the bar's surface. The pO_2 during measurements was controlled by mixing oxygen and nitrogen or CO_2 and CO in the desired ratios using Brooks GF40 mass flow controllers (Brooks Instruments Inc.).

Conflicts of interest

The authors declare no conflicts of interest.

Acknowledgements

Financial support from the Dutch Technology Foundation (STW, now part of NWO; Project No. 15325) is gratefully acknowledged.

References

1 A. Atkinson, S. Barnett, R. J. Gorte, J. Irvine, A. J. McEvoy, M. Mogensen, S. C. Singhal and J. Vohs, *Nat. Mater.*, 2004, **3**, 17–27.
2 S. P. Jiang and S. H. Chan, *J. Mater. Sci.*, 2004, **39**, 4405–4439.
3 A. Hauch, R. Küngas, P. Blennow, A. B. Hansen, J. B. Hansen, B. V. Mathiesen and M. B. Mogensen, *Science*, 2020, **370**, eaba6118.
4 Y. Zheng, W. Zhang, Y. Li, J. Chen, B. Yu, J. Wang, L. Zhang and J. Zhang, *Nano Energy*, 2017, **40**, 512–539.
5 S. D. Ebbesen, S. H. Jensen, A. Hauch and M. B. Mogensen, *Chem. Rev.*, 2014, **114**, 10697–10734.
6 Y. Song, X. Zhang, K. Xie, G. Wang and X. Bao, *Adv. Mater.*, 2019, **31**, 1902033.
7 X. Yue and J. T. S. Irvine, *J. Electrochem. Soc.*, 2012, **159**, F442–F448.
8 P. I. Cowin, C. T. Petit, R. Lan, J. T. Irvine and S. Tao, *Adv. Energy Mater.*, 2011, **1**, 314–332.
9 Y. Jiang, Y. Yang, C. Xia and H. J. M. Bouwmeester, *J. Mater. Chem. A*, 2019, **7**, 22939–22949.
10 C. Graves, S. D. Ebbesen, S. H. Jensen, S. B. Simonsen and M. B. Mogensen, *Nat. Mater.*, 2015, **14**, 239–244.
11 Z. Gao, L. V. Mogni, E. C. Miller, J. G. Railsback and S. A. Barnett, *Energy Environ. Sci.*, 2016, **9**, 1602–1644.
12 G. Tsekouras, D. Neagu and J. T. S. Irvine, *Energy Environ. Sci.*, 2013, **6**, 256–266.
13 W. Jung, J. O. Dereux, W. C. Chueh, Y. Hao and S. M. Haile, *Energy Environ. Sci.*, 2012, **5**, 8682–8689.
14 X. Zhang, Y. Song, F. Guan, Y. Zhou, H. Lv, Q. Liu, G. Wang and X. Bao, *J. Power Sources*, 2018, **400**, 104–113.
15 F. Bidrawn, G. Kim, G. Corre, J. Irvine, J. M. Vohs and R. J. Gorte, *Electrochem. Solid-State Lett.*, 2008, **11**, B167.

16 L. Ye, C. Pan, M. Zhang, C. Li, F. Chen, L. Gan and K. Xie, *ACS Appl. Mater. Interfaces*, 2017, **9**, 25350–25357.
17 G. Tsekouras and J. T. S. Irvine, *J. Mater. Chem.*, 2011, **21**, 9367–9376.
18 W. Qi, Y. Gan, D. Yin, Z. Li, G. Wu, K. Xie and Y. Wu, *J. Mater. Chem. A*, 2014, **2**, 6904–6915.
19 J. H. Zhang, F.-Z. Han, C.-X. Li and S.-L. Zhang, *J. Eur. Ceram. Soc.*, 2022, **42**, 5801–5812.
20 A. K. Opitz, A. Nenning, C. Rameshan, M. Kubicek, T. Götsch, R. Blume, M. Hävecker, A. Knop-Gericke, G. n. Rupprechter and B. Klötzer, *ACS Appl. Mater. Interfaces*, 2017, **9**, 35847–35860.
21 Y. Zhou, Z. Zhou, Y. Song, X. Zhang, F. Guan, H. Lv, Q. Liu, S. Miao, G. Wang and X. Bao, *Nano Energy*, 2018, **50**, 43–51.
22 Y. Li, Y. Li, Y. Wan, Y. Xie, J. Zhu, H. Pan, X. Zheng and C. Xia, *Adv. Energy Mater.*, 2019, **9**, 1803156.
23 Y. Q. Zhang, J. H. Li, Y. F. Sun, B. Hua and J. L. Luo, *ACS Appl. Mater. Interfaces*, 2016, **8**, 6457–6463.
24 J. Zhang, K. Xie, H. Wei, Q. Qin, W. Qi, L. Yang, C. Ruan and Y. Wu, *Sci. Rep.*, 2014, **4**, 7082.
25 Đ. Tripković, J. Wang, R. Küngas, M. B. Mogensen, B. Yildiz and P. V. Hendriksen, *Chem. Mater.*, 2022, **34**, 1722–1736.
26 C. Zhang, J. Sunarso and S. Liu, *Chem. Rev.*, 2017, **46**, 2941–3005.
27 B. Koo, K. Kim, J. K. Kim, H. Kwon, J. W. Han and W. Jung, *Joule*, 2018, **2**, 1476–1499.
28 R. Price, J. G. Grolig, A. Mai and J. T. S. Irvine, *Solid State Ionics*, 2020, **347**.
29 P. Kim-Lohsoontorn and J. Bae, *J. Power Sources*, 2011, **196**, 7161–7168.
30 V. Singh, H. Muroyama, T. Matsui, S. Hashigami, T. Inagaki and K. Eguchi, *J. Power Sources*, 2015, **293**, 642–648.
31 C. Gaudillere, L. Navarrete and J. M. Serra, *Int. J. Hydrogen Energy*, 2014, **39**, 3047–3054.
32 S. Wang, T. Kobayashi, M. Dokiya and T. Hashimoto, *J. Electrochem. Soc.*, 2000, **147**, 3606–3609.
33 R. Schmitt, A. Nenning, O. Kraynis, R. Korobko, A. I. Frenkel, I. Lubomirsky, S. M. Haile and J. L. Rupp, *Chem. Soc. Rev.*, 2020, **49**, 554–592.
34 W. C. Chueh, Y. Hao, W. Jung and S. M. Haile, *Nat. Mater.*, 2011, **11**, 155–161.
35 A. Nenning, M. Holzmann, J. Fleig and A. K. Opitz, *Mater. Adv.*, 2021, **2**, 5422–5431.
36 T. L. Skafte, Z. Guan, M. L. Machala, C. B. Gopal, M. Monti, L. Martinez, E. Stamate, S. Sanna, J. A. Garrido Torres, E. J. Crumlin, M. García-Melchor, M. Bajdich, W. C. Chueh and C. Graves, *Nat. Energy*, 2019, **4**, 846–855.
37 B. A. Boukamp, *Solid State Ionics*, 1986, **18**, 136–140.
38 B. De Boer, PhD thesis, University of Twente, Enschede, The Netherlands, 1998.
39 J. Bisquert, G. Garcia-Belmonte, F. Fabregat-Santiago and A. Compte, *Electrochem. Commun.*, 1999, **1**, 429–435.
40 D. Chen, S. R. Bishop and H. L. Tuller, *ECS Trans.*, 2013, **57**, 1387.
41 W. Lai and S. M. Haile, *J. Am. Ceram. Soc.*, 2005, **88**, 2979–2997.
42 J. S. Lee, J. Jamnik and J. Maier, *Monatsh. Chem.*, 2009, **140**, 1113–1119.
43 S. R. Bishop, K. L. Duncan and E. D. Wachsman, *Acta Mater.*, 2009, **57**, 3596–3605.
44 S. Park, Y. Kim, H. Han, Y. S. Chung, W. Yoon, J. Choi and W. B. Kim, *Appl. Catal., B*, 2019, **248**, 147–156.
45 S. Park, H. Han, W. Yoon, J. Choi, Y. Kim, H. Kim and W. B. Kim, *ACS Sustainable Chem. Eng.*, 2020, **8**, 6564–6571.
46 S. Wang, H. Jiang, Y. Gu, B. Yin, S. Chen, M. Shen, Y. Zheng, L. Ge, H. Chen and L. Guo, *Electrochim. Acta*, 2020, **337**, 135794.
47 S. Liu, Q. Liu and J.-L. Luo, *J. Mater. Chem. A*, 2017, **5**, 2673–2680.
48 P. Addo, B. Molero-Sanchez, M. Chen, S. Paulson and V. Birss, *Fuel cells*, 2015, **15**, 689–696.
49 S. Bishop, K. Duncan and E. Wachsman, *Electrochim. Acta*, 2009, **54**, 1436–1443.
50 S. Grieshammer and M. Martin, *J. Mater. Chem. A*, 2017, **5**, 9241–9249.
51 S. Grieshammer, *Phys. Chem. Chem. Phys.*, 2021, **23**, 10321–10325.
52 A. Shaur and H. J. M. Bouwmeester, to be published.
53 T. Kawada, J. Suzuki, M. Sase, A. Kaimai, K. Yashiro, Y. Nigara, J. Mizusaki, K. Kawamura and H. Yugami, *J. Electrochem. Soc.*, 2002, **149**, E252.
54 A. Schmid, G. M. Rupp and J. Fleig, *Phys. Chem. Chem. Phys.*, 2018, **20**, 12016–12026.
55 Z. A. Feng, M. L. Machala and W. C. Chueh, *Phys. Chem. Chem. Phys.*, 2015, **17**, 12273–12281.
56 Y. Yu, B. Mao, A. Geller, R. Chang, K. Gaskell, Z. Liu and B. W. Eichhorn, *Phys. Chem. Chem. Phys.*, 2014, **16**, 11633–11639.
57 W. Taifan, J.-F. Boily and J. Baltrusaitis, *Surf. Sci. Rep.*, 2016, **71**, 595–671.

